

NUMERICAL PREDICTION AND EXPERIMENTAL VALIDATION ON THRUST PERFORMANCE OF SCRAMJET EXTERNAL NOZZLES

Tatsushi Isono[1]

[1]Japan Aerospace Exploration Agency

Abstract

A Scramjet External Nozzle (SEN) is a promising candidate for the nozzle element of hypersonic airbreathing propulsion systems because it can improve both thrust-to-weight and lift-to-drag characteristics through airframe-propulsion integration. For conceptual design of scramjet engines with SEN configurations, a practical prediction method for nozzle thrust performance is required. In the present study, Computational Fluid Dynamics (CFD) simulations and wind-tunnel experimental validation were conducted to evaluate the thrust-related pressure load of an SEN with reasonable computational cost. In an SEN configuration, the cowl is truncated to reduce nozzle weight while maintaining the expansion area, and the nozzle exhaust flow directly interacts with the ambient flow through the jet boundary. The open-source CFD package OpenFOAM v2412, ESI-OpenCFD distribution, was employed for the present Reynolds-averaged Navier-Stokes (RANS) simulations. The validation experiment was conducted using the Pilot Wind Tunnel (PWT). The ramp-wall pressure distribution and its line-integrated pressure quantity were used as validation data. The comparison between computation and experiment shows that the present simulation reproduces the dominant nozzle–ambient flow interaction and its effect on the ramp-wall pressure distribution over a wide range of Nozzle Pressure Ratio (*NPR*). The thrust-related integrated pressure quantity was predicted within an error of 7% for all test conditions. Each case was completed in approximately 15 min using a laptop computer equipped with an Intel Core Ultra 7 165H CPU and 64 GB RAM, running Windows 11 with WSL2 and Ubuntu Linux. These results indicate that the present CFD framework provides a practical balance between prediction accuracy and computational cost for preliminary SEN design.

Keywords: scramjet engine, scramjet external nozzle, wind tunnel test, computational fluid dynamics

1. Introduction

Scramjet propulsion systems are one of the most promising technologies for sustained hypersonic flight because they maintain supersonic flow throughout the entire engine flowpath, enabling high specific impulse at Mach numbers above approximately 5 [1]. In hypersonic airbreathing propulsion systems, airframe-propulsion integration (API) is essential to achieve both high thrust-to-weight and lift-to-drag ratios. For this purpose, the nozzle element of a scramjet engine often adopts a Single Expansion Ramp Nozzle (SERN) configuration [2]. To further improve the aerodynamic and structural efficiency of the propulsion system, the cowl on the opposite side of the expansion ramp is partially or entirely truncated in many practical designs. Such a configuration is generally referred to as a Scramjet External Nozzle (SEN) [3]. Figure 1 denotes the components of scramjet engine system and nozzle element,

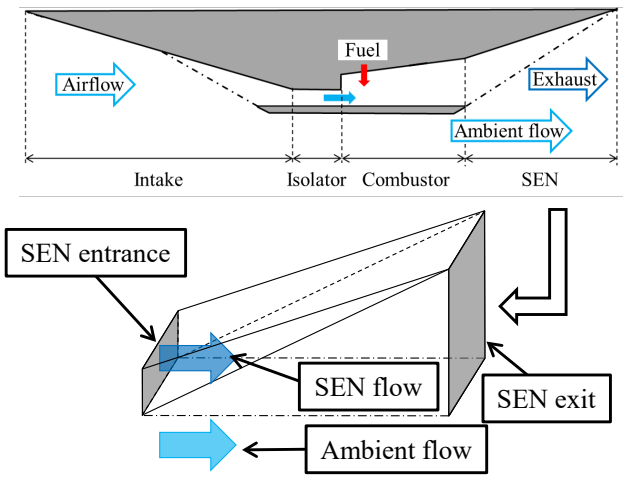


Figure 1 – Schematics of scramjet engine and SEN.

viz. SEN. This engine is composed of intake, isolator, combustor, and nozzle aligned from upstream to downstream in this order. In SEN configurations, the nozzle exhaust flow directly interacts with the ambient external flow through the jet boundary because of the open nozzle structure. As a result, the nozzle thrust performance strongly depends not only on the internal nozzle expansion process but also on the aerodynamic interaction between the engine exhaust and the surrounding flowfield.

Various studies have been conducted on scramjet nozzles and SERN configurations [4-8]. However, investigations focusing on the interaction between nozzle exhaust flow and ambient flow over a wide range of operating conditions are still limited. Previous experimental investigations by the present author demonstrated that the interaction structure between these two supersonic flows significantly affects the pressure distribution and thrust performance of SEN configurations depending on the Nozzle Pressure Ratio (*NPR*) and nozzle geometry [9].

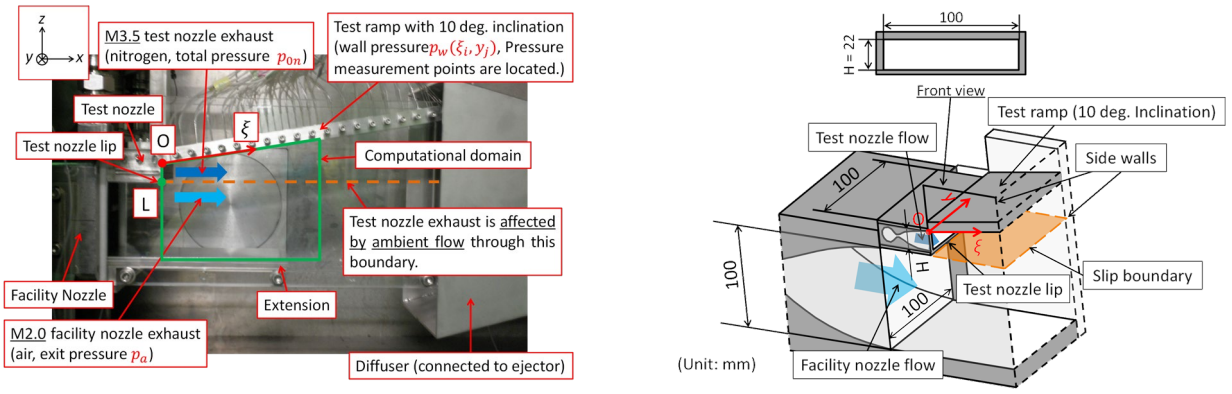
For practical conceptual design of hypersonic propulsion systems, rapid and reasonably accurate prediction methods for SEN aerodynamic performance are required. Although high-fidelity computational approaches such as Large-Eddy Simulation (LES) and Direct Numerical Simulation (DNS) can provide detailed flow physics, their computational cost is generally impractical for iterative engineering design studies. Therefore, Reynolds-Averaged Navier-Stokes (RANS)-based Computational Fluid Dynamics (CFD) methods are expected to provide a suitable balance between prediction accuracy and computational efficiency for preliminary SEN design applications. Such engineering CFD allows us to use commercial personal computer for computational resources instead of supercomputers. In a previous preliminary study [10], the present author applied two-dimensional Euler CFD simulations to experimentally validated SEN flowfields and confirmed that the qualitative characteristics of pressure-wave structures and ramp-wall pressure distributions could be reproduced with relatively low computational cost. However, significant discrepancies remained in the quantitative prediction of wall pressure distributions because viscous effects, including boundary layers and shear-layer mixing between the nozzle jet and ambient flow, were neglected in the Euler formulation.

The objective of the present study is to extend the previous preliminary CFD framework to viscous RANS simulations and to investigate its applicability as a practical engineering prediction tool for SEN aerodynamic performance. Wind tunnel experiments were conducted, and the computational results were validated against experimentally measured ramp-wall pressure distributions and their line-integrated quantities related to nozzle thrust performance. Particular attention is focused on the interaction structure between the nozzle exhaust flow and ambient flow under over-expanded, approximately-optimum-expanded, and under-expanded operating conditions. In addition, the prediction accuracy and computational cost of the present RANS approach are discussed from the viewpoint of practical preliminary design applications.

2. Experimental Validation Test

2.1 Experimental Setup

Validation experiments were conducted using the Pilot Wind Tunnel (PWT) [11] located at the Kakuda



a – Side view photograph.

b – Schematic sketch.

Figure 2 – Test section.

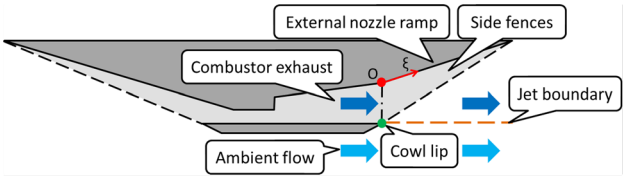


Figure 3 – Schematic sketch for actual engine system.

Table 1 – Components correspondence.

Experiment	Actual engine
Test nozzle exhaust	Engine exhaust
Facility nozzle exhaust	Ambient flow
Test ramp	SEN ramp wall
Test nozzle lip	Cowl lip
Rectangle side walls	Side fences

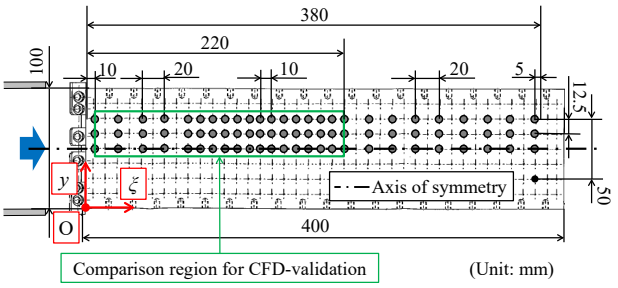


Figure 4 – Pressure measurement locations on test ramp surface.

Space Center of the Japan Aerospace Exploration Agency (JAXA). The PWT is a long-duration blow-down type supersonic wind tunnel composed mainly of an air supply line, an ejector line, and a low-pressure chamber placed between these two lines. The test section was installed inside the low- pressure chamber. During the test operation, the chamber was first evacuated by the ejector system, and then compressed air was discharged from the facility nozzle into the test section.

Figure 2 shows a photograph and schematic illustration of the test section. In the present configuration, a test nozzle was mounted continuously along the upper inner wall of the facility nozzle. The facility nozzle supplied a Mach 2.0 air flow, while the test nozzle supplied a Mach 3.5 nitrogen flow. The experiments were conducted under room-temperature, non-reacting conditions because the present study focuses on the aerodynamic interaction between the nozzle exhaust flow and the external ambient flow, rather than on combustion or real-gas effects. A test ramp was installed downstream of the test nozzle. The test ramp was connected continuously to the upper inner wall of the test nozzle and inclined by 10 degrees relative to the test-nozzle axis. The flows discharged from the facility nozzle and the test nozzle interacted with each other downstream of the test nozzle lip, which corresponds to the finite-thickness lower wall of the test nozzle. Rectangular side walls were installed on both sides of the test section to suppress excessive spanwise expansion of the flowfield.

Figure 3 describes an actual Scramjet External Nozzle (SEN) system. Table 1 summarizes the relationship between the experimental components and the corresponding components of an actual engine configuration. The test nozzle exhaust and the facility nozzle exhaust respectively simulate the engine exhaust flow and the ambient external flow of an actual SEN. The test ramp corresponds to the SEN expansion ramp wall, while the test nozzle lip models the cowl lip of the external nozzle. The rectangular side walls in the experiment represent the side fences of an actual SEN configuration. It should be noted that the Mach numbers adopted in the present experiment were not selected to reproduce a specific flight condition. Instead, they were determined by considering the capability of the wind tunnel facility and by ensuring that both the test-nozzle and facility-nozzle flows remained supersonic. This configuration was selected so that pressure-wave structures such as expansion waves, compression waves, and shock waves could be clearly generated and repeatedly reflected within the test section.

2.2 Measurements and Data Reduction

The ramp-wall pressure distribution was measured to evaluate the aerodynamic performance of the SEN model and to provide validation data for the CFD simulations. As shown Fig. 4, the wall pressure was measured over the ramp surface in both streamwise and spanwise directions. The present CFD analysis was two-dimensional without spanwise direction so that the ramp-wall pressure distribution derived from CFD was one-dimensional. To compare these one-dimensional data with two-dimensional experimental ones, a Spanwise Averaged Pressure Distribution (SAPD) [9] was defined as formulated in Eq (1).

$$\begin{cases} y_j = 75 - 12.5(j-1) \\ \left(\frac{p_{wave}}{p_{0n}}\right)(\xi) = \frac{1}{p_{0n}}\left\{\frac{1}{5}\cdot\sum_{j=1}^{5} p_w(\xi, y_j)\right\} \end{cases} \quad (1)$$

The SAPD is streamwise ramp-wall pressure distribution normalized by test nozzle total pressure of p_{0n}, which is averaged in spanwise direction at each streamwise coordinate. The following standard deviation quantifying spanwise pressure variation was also calculated and utilized as error bars in SAPD graphs.

$$\sigma_y(\xi) = \sqrt{\frac{1}{5}\cdot\sum_{j=1}^{5}\left\{\left(\frac{p_w}{p_{0n}}\right)(\xi, y_j) - \left(\frac{p_{wave}}{p_{0n}}\right)(\xi)\right\}^2} \quad (2)$$

The SAPD with error bar (Eqs. (1) and (2)) was used as the primary validation quantity for the CFD results. In addition, the line integral of the SAPD, denoted here as C_p (Eq. (3)), was used as a thrust-related integrated quantity. The CFD prediction capability was therefore assessed not only from the local wall-pressure distribution but also from this integrated pressure quantity.

$$C_p = \frac{1}{p_{0n}\cdot H}\int p_{wave}(\xi)\, d\xi \quad (3)$$

In addition, C_p prediction errors, *PE*, were derived as percentage quantities, as follows.

$$PE = 100\cdot\frac{\left|C_{pexp} - C_{pcfd}\right|}{C_{pexp}} \quad (4)$$

2.3 Test Conditions

The experimental condition was characterized by the *NPR*, defined as,

$$NPR = \frac{p_{0n}}{p_{ae}} \quad (5)$$

where p_{0n} is the total pressure of the test nozzle and p_{ae} is the static pressure at the facility nozzle exit. In the present experiment, *NPR* defines the expansion condition of the test-nozzle jet. In an actual SEN configuration, this parameter corresponds to the expansion state of the engine exhaust flow relative to the ambient external flow. Since the exit Mach number of the test nozzle was 3.5, the optimum *NPR* for the test-nozzle jet was estimated to be 76.0 under the present conditions. Therefore, the test-nozzle jet is over-expanded when *NPR* is lower than 76.0, and under-expanded when *NPR* is higher than 76.0. In this study, the range of *NPR*=76.0±5.0, namely from 71.0 to 81.0, was regarded

Table 2 – Validation test condition.

Case	Expansion condition	p_{0n}, kPa	p_{ae}, kPa	*NPR*
1	Over	630	23.5	26.8
2		629	17.4	36.3
3		628	14.1	44.4
4		627	11.2	55.8
5		626	9.45	66.3
6	Approximately-optimum	625	8.58	72.9
7		625	7.76	80.5
8	Under	624	6.99	89.2
9		623	6.29	99.1
10		623	5.64	110.4
11		622	5.08	122.5

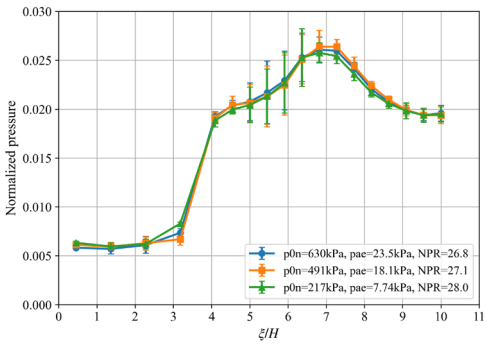


Figure 5 – Comparison of ramp-wall pressure distributions for nearly identical *NPR* with different p_{0n} and p_{ae}.

as the approximately-optimum-expanded condition.

Under over-expanded conditions, the static pressure of the test-nozzle jet is lower than that of the facility-nozzle flow at the nozzle exit. As a result, a shock wave is generated on the test-nozzle jet side from the nozzle lip, while an expansion wave is generated on the facility-nozzle flow side. Conversely, under under-expanded conditions, an expansion wave is generated on the test-nozzle jet side, while a shock wave is generated on the facility-nozzle flow side. Under an completely optimum-expanded condition (*NPR*=76.0), no strong pressure wave is expected to be generated from the nozzle lip. In the actual experiment, however, weak expansion and recompression waves may still appear because of the finite thickness of the nozzle lip and the associated base-flow region. The *NPR* range was varied as widely as possible within the operational capability of the wind tunnel. During one wind-tunnel run, the total pressure of the test nozzle was kept approximately constant, while the facility-nozzle exit pressure was varied by adjusting the valve opening of the wind tunnel system. In this way, experimental data for multiple *NPR* conditions were obtained in a single run. The test conditions are summarized in Table 2.

Under under-expanded conditions, the ramp-wall pressure tends to decrease due to the expansion wave generated from the test nozzle lip. As *NPR* increases, the static-pressure difference between the test-nozzle jet and the facility-nozzle flow becomes larger, resulting in a stronger pressure decrease on the ramp wall. In addition, when an oblique shock wave reflected from the jet boundary impinges on the ramp wall, a strong adverse pressure gradient can be formed. In the downstream region of the ramp, a pressure rise associated with possible shock-induced flow separation was observed in the experiment. The present study focuses on the nozzle–ambient flow interaction and its effect on the ramp-wall pressure distribution before the onset of such downstream separation effects. Therefore, the comparison between the experiment and CFD was restricted to the upstream region of the test ramp indicated in Fig. 2a. This region corresponds to the streamwise ramp coordinate up to approximately 220 mm from the test-nozzle exit, which is highlighted in Fig. 4.

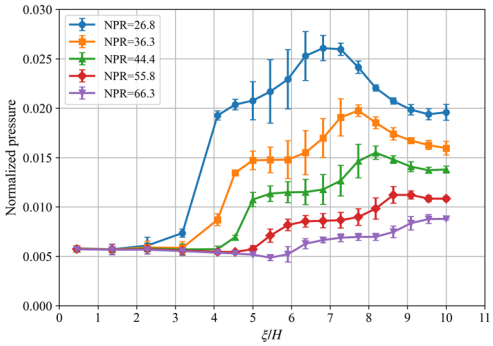
Table 3 – C_p differences among approximately equal *NPR* cases.

p_{0n}, kPa	p_{ae}, kPa	*NPR*	C_p
630	23.5	26.8	0.1599
491	18.1	27.1	0.1599
217	7.74	28	0.1595

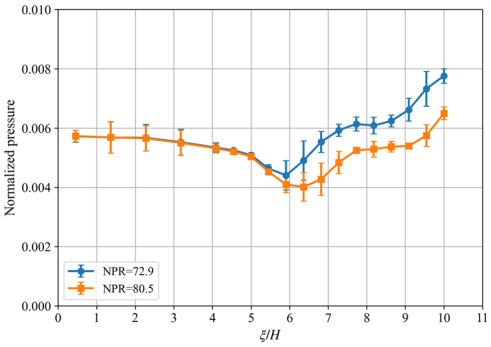
2.4 Validation Data

Before using the present experimental results as validation data for the CFD simulations, the repeatability and similarity of the ramp-wall pressure distribution were examined. Figure 5 shows the streamwise distributions of the normalized ramp-wall pressure, defined as SAPD in Eq. (1), for three different wind-tunnel runs conducted under nearly identical *NPR* conditions. Error bars are standard deviation as described in Eq. (2). In these cases, the total pressure of the test nozzle, p_{0n}, and the facility-nozzle exit pressure, pae, were varied significantly. Specifically, p_{0n} ranged from 217 to 630 kPa, and p_{ae} ranged from 7.74 to 23.5 kPa. Nevertheless, the corresponding *NPR* values remained close to each other, ranging from 26.8 to 28.0. As shown in Fig. 5, the three pressure distributions almost collapse onto a single curve when the wall pressure is normalized by the test-nozzle total pressure. The initial pressure level, the rapid pressure rise downstream of the ramp expansion region, the peak pressure location, and the subsequent pressure recovery trend are all reproduced consistently among the three runs. This result indicates that the ramp-wall pressure distribution is primarily governed by *NPR*, rather than by the absolute values of p_{0n} and p_{ae}, under the present experimental configuration.

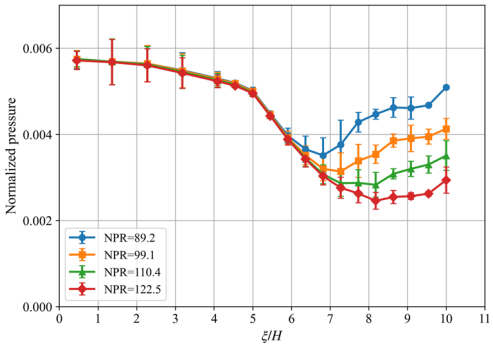
The repeatability was also confirmed using the normalized pressure integration quantity, C_p derived from Eq. (3), which is used in the present study as a thrust-related validation metric. Table 3 summarizes the C_p differences for each case. The obtained C_p values are identical up to the third decimal place when rounded to three decimal digits, namely C_p=0.160. Therefore, the present



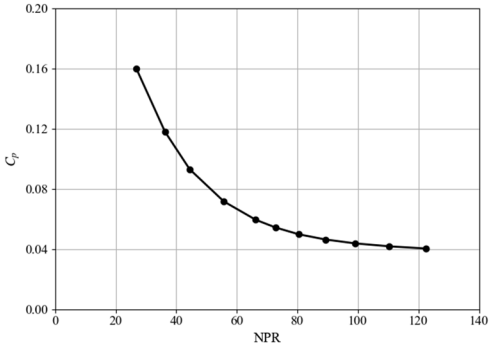
a – Ramp-wall pressure distributions under over-expanded conditions.



b – Ramp-wall pressure distributions under approximately-optimum-expanded conditions.



c – Ramp-wall pressure distributions under under-expanded conditions.



d – Relation between C_p and *NPR*.

Figure 6 – Experimental results for CFD validation.

experimental data are considered sufficiently repeatable for the validation of the CFD prediction of both the local ramp-wall pressure distribution and the integrated pressure quantity. Based on this confirmation, the ramp-wall pressure distributions and the corresponding C_p values obtained under each *NPR* condition were used as the validation data for the numerical simulations. Figure 6 shows the experimental results for CFD validation. The ramp-wall pressure distributions are arranged in each expansion condition. The relation between C_p and *NPR* is also employed for validation, mainly utilized for quantification of nozzle thrust performances.

3. Numerical Simulation

3.1 Computational Method

Numerical simulations were performed using the open-source computational fluid dynamics package OpenFOAM v2412, ESI-OpenCFD distribution. The density-based compressible solver rhoCentralFoam was employed because the present flowfield includes shock waves, expansion waves, and their repeated reflections between the ramp wall and the jet boundary. In contrast to the previous preliminary Euler simulations [10], the present study solved the compressible RANS equations to include viscous and turbulent effects on the nozzle-ambient flow interaction. Numerical setup is tabulated in Table 4. The gas was approximated as a single calorically perfect gas, simulating air. A specific heat at constant pressure of c_p=1005 J/(kg·K), a molecular weight of 28.96, a constant molecular viscosity of μ=1.8×10^{-5} Pa·s, and a Prandtl number of 0.72 were adopted. In the present simulation, however, both flows were treated as air because the standard rhoCentralFoam framework used in this study does not solve multi-species transport. This simplification was considered acceptable for the present objective, since the study focuses on the aerodynamic pressure-wave interaction and the ramp-wall pressure distribution under non-reacting room-temperature conditions, rather than on molecular mixing or species-concentration fields. The possible influence of the gas-property difference between air and nitrogen is therefore included in the modeling uncertainty of the present CFD validation.

Turbulence was modeled using the shear-stress transport *k*-ω model. This model was selected

Table 4 – Numerical setup.

Item	Description
CFD code	OpenFOAM v2412, ESI-OpenCFD distribution
Solver	rhoCentralFoam
Governing equations	Compressible RANS equations
Turbulence model	SST k-ω model
Gas model	Single calorically perfect gas, air properties
Thermodynamic model	c_p=1005 J/(kg·K), molecular weight = 28.96
Molecular viscosity	μ=1.8×10^{-5} Pa·s
Prandtl number	0.72
Dimensionality	Two-dimensional
Spanwise boundary	empty
Inlet boundary conditions	Fixed static pressure, velocity, and static temperature
Outlet and lower boundaries	Zero-gradient
Wall boundary condition	No-slip adiabatic wall
Wall treatment	Wall functions for turbulent quantities
Flux scheme	Tadmor central-upwind scheme
Time discretization	First-order Euler scheme
Time-step control	Adaptive time step
Maximum Courant number	0.13
End time	2.0×10^{-3} s
Mesh generation	blockMesh
Grid type	Structured hexahedral mesh

because it is widely used for compressible wall-bounded flows, including shock-wave/boundary-layer interaction, and provides a practical balance between robustness and computational cost. The convective fluxes were evaluated using the central-upwind scheme implemented in rhoCentralFoam, and the Tadmor flux scheme was adopted. First-order Euler time discretization was used, and the time step was automatically adjusted based on the Courant number. The maximum Courant number was set to 0.13. Each calculation was advanced up to 2.0×10^{-3} s, by which the ramp-wall pressure distribution reached a quasi-steady state suitable for comparison with the experimental data.

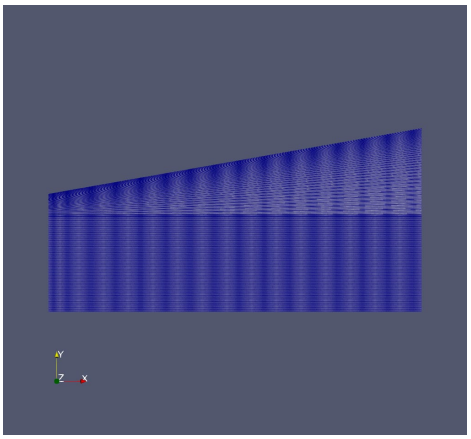


Figure 7 – Computational domain covered by medium-scale mesh.

3.2 Computational Domain and Boundary Conditions

The computational domain was constructed to reproduce the streamwise cross-section of the experimental test section. Figure 7 shows the computational domain. This is a medium mesh configuration described later. The test ramp was connected continuously to the upper wall of the test nozzle and inclined by 10 degrees, as in the experiment. The computational domain covered the entire ramp length, whereas the comparison between computation and experiment was limited to the upstream portion of the ramp described in section 2.4, in order to avoid the influence of downstream separation observed in the experiment.

A two-dimensional flowfield was assumed by applying an empty boundary condition to the front and back planes in the spanwise direction. The facility-nozzle exit and the test-nozzle exit were treated as inlet boundaries. Fixed values of static pressure, velocity, and static temperature were imposed at these boundaries. These inlet quantities were determined from the wind-tunnel operating conditions and the nominal nozzle expansion conditions. The downstream outlet and the lower boundary were specified using zero-gradient conditions. The test ramp wall and the test-nozzle lip were treated as no-slip adiabatic walls. Wall functions were applied to the turbulent quantities on the solid-wall boundaries. The ramp-wall pressure distribution was sampled from the testRampWall boundary

during the calculation. The sampled wall pressure was normalized by the test-nozzle total pressure, *p0n*, and compared with the experimental pressure distribution, that is, SAPD.

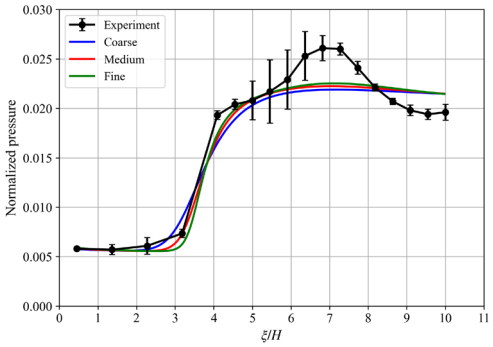


Figure 8 – Effect of mesh resolution on the normalized ramp-wall pressure distribution for a representative over-expanded condition.

3.3 Computational Mesh

The mesh was generated using blockMesh. A structured hexahedral mesh was adopted to maintain a simple and robust grid topology for the present two-dimensional nozzle flowfield. The computational domain was divided into several blocks corresponding to the facility-nozzle flow region, the test-nozzle lip region, and the test-ramp region. Grid clustering was applied near the solid walls and around the nozzle-lip region so that the boundary layer, the rapid pressure variation caused by the ramp expansion, and the reflected pressure waves could be captured with sufficient resolution. Three mesh resolutions were prepared for the mesh-sensitivity study: coarse, medium, and fine meshes. The numbers of cells were approximately 1.8×10^4, 5.0×10^4, and 1.1×10^5, respectively. The medium mesh (Fig. 7), consisting of approximately 5.0×10^4 cells, was used for the main validation calculations after confirming that further refinement produced only a small change in the ramp-wall pressure distribution and the integrated pressure quantity, as explained in the next paragraph.

Figure 8 shows the effect of mesh resolution on the normalized ramp-wall pressure distribution for a representative over-expanded condition, case 1. The experimental data are also shown for comparison. All three computational meshes reproduced the major trend of the pressure distribution, including the rapid pressure rise downstream of the initial ramp expansion and the gradual pressure recovery in the downstream region. The difference among the three computational results was much smaller than the discrepancy between the computation and the experiment. The line-integrated pressure quantity, denoted as C_p (Eq. (3)), was also compared among the three meshes. The C_p related values are summarized in Table 5. The obtained C_p values were 0.152, 0.153, and 0.154 for the coarse, medium, and fine meshes, respectively. Correspondingly the prediction errors from experimental value were 5.1 %, 4.5 %, and 4.1 %. The relative difference between the medium and fine meshes was approximately 0.45 %, while that between the coarse and fine meshes was approximately 1.1 %. Therefore, the numerical result was considered sufficiently insensitive to the mesh resolution for the purpose of the present validation study. The computational time, however, increased significantly with grid refinement. The required wall-clock times were approximately 273 s, 890 s, and 3122 s for the coarse, medium, and fine meshes, respectively. The medium mesh required approximately 15 min per case and provided a reasonable compromise between prediction accuracy and computational cost. Therefore, the medium mesh was selected for the following validation calculations.

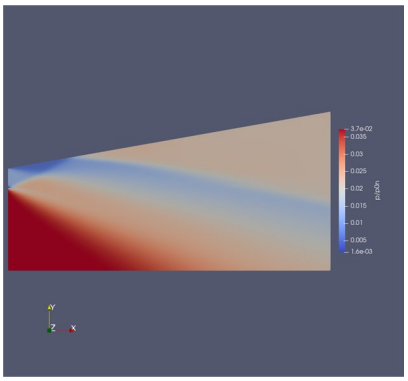
Table 5 – Mesh sensitivity study.

Case	Number of cells	Wall-clock time [s]	C_p	*PE* [%]	Diff. from fine [%]
Experiment	-	-	0.160	-	-
Coarse mesh	1.8×10^4	273	0.152	5.1	1.1
Medium mesh	5.0×10^4	890	0.153	4.5	0.45
Fine mesh	1.1×10^5	3122	0.154	4.1	-

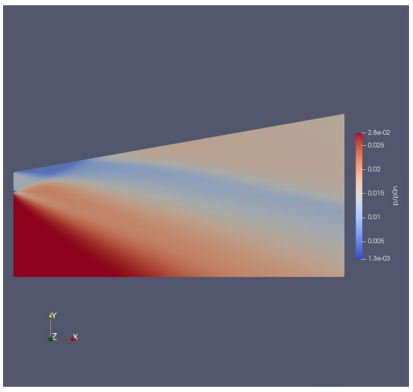
4. Validation Results and Discussion

4.1 Flowfield Structure

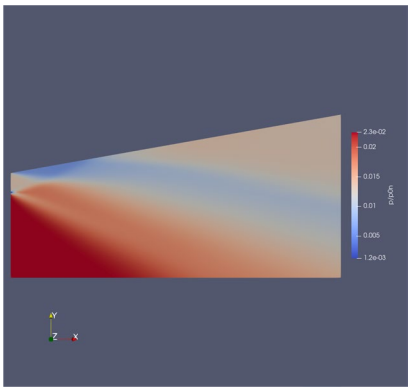
Figure 9 shows the normalized static-pressure contours obtained by the present RANS simulations for the *NPR* conditions investigated in this study. The pressure was normalized by the test-nozzle total pressure, p_{0n}. Although no flow visualization was conducted in the wind-tunnel experiment, these



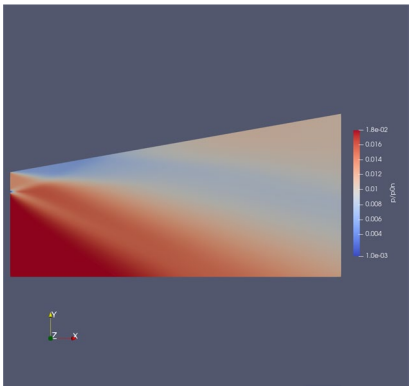
a – Cae 1, *NPR*=26.8.



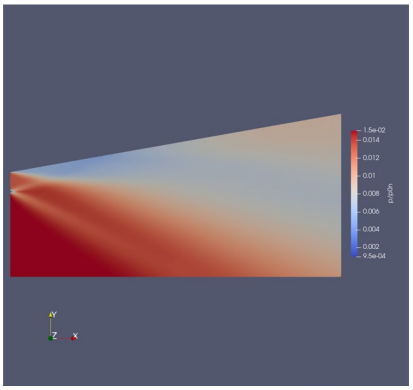
b – Cae 2, *NPR*=36.3.



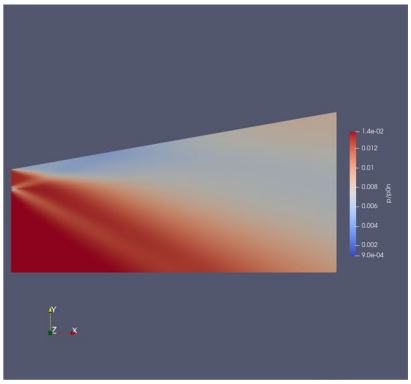
c – Cae 3, *NPR*=44.4.



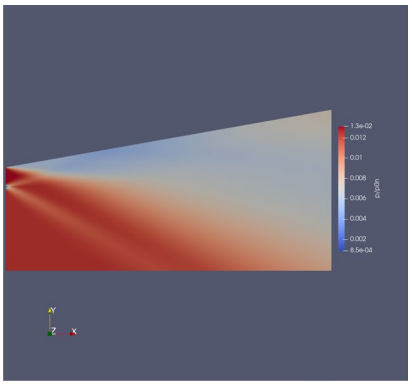
d – Cae 4, *NPR*=55.8.



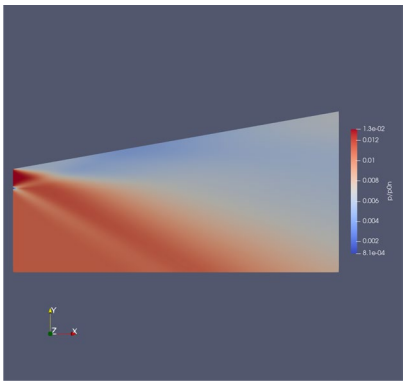
e – Cae 5, *NPR*=66.3.



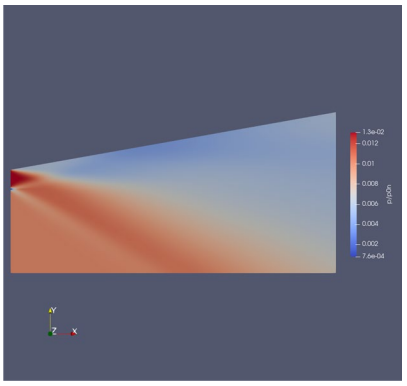
f – Cae 6, *NPR*=72.9.



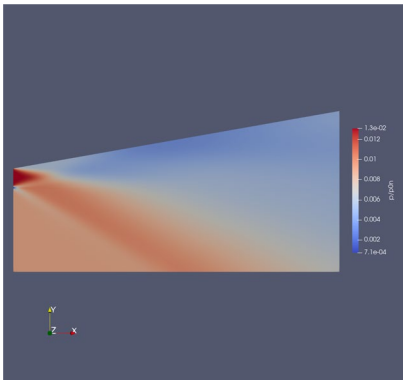
g – Cae 7, *NPR*=80.5.



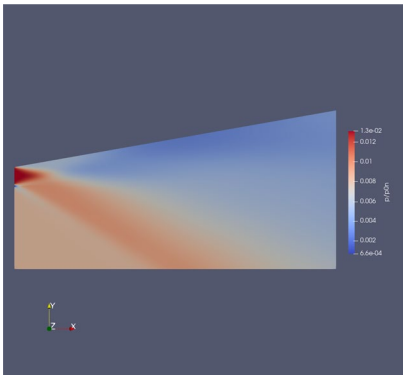
h – Cae 8, *NPR*=89.2.



i – Cae 9, *NPR*=99.1.



j – Cae 10, *NPR*=110.4.



k – Cae 11, *NPR*=122.5.

Figure 9 – Normalized static-pressure contours obtained by the present RANS simulations.

contours are useful for interpreting the pressure-wave structures responsible for the measured ramp-wall pressure distributions.

The computed flowfields clearly show the interaction between the test-nozzle exhaust and the facility-nozzle flow downstream of the test-nozzle lip. Depending on *NPR*, different pressure-wave systems are formed near the nozzle lip and propagate toward the ramp wall and the jet boundary. Under over-expanded conditions (cases 1 to 5), the test-nozzle jet is compressed by the surrounding facility-nozzle flow, and a compression-wave or shock-wave system is generated on the test-nozzle side. This wave system impinges on the ramp wall and causes a rapid increase in the wall pressure. In contrast, under under-expanded conditions, the test-nozzle jet expands toward the facility-nozzle flow, and an expansion-wave system is generated from the nozzle-lip region. This produces a gradual decrease in the ramp-wall pressure downstream of the nozzle exit.

For *NPR* values close to the approximately optimum-expanded condition, the pressure difference between the test-nozzle jet and the facility-nozzle flow becomes relatively small. Consequently, the pressure waves generated from the nozzle-lip region are weaker than those observed in the over-expanded and under-expanded cases. The computed pressure contours therefore indicate that the present RANS simulation qualitatively reproduces the expected change in the nozzle-ambient interaction structure with *NPR*.

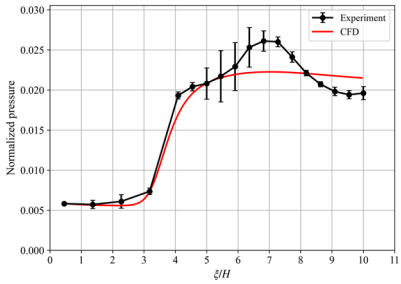
Compared with the previous Euler calculation [10], the present viscous simulation also provides a more physically realistic representation of the wall-bounded flow. The no-slip ramp wall and turbulent shear layer between the two supersonic streams lead to smoother pressure transitions and weaker numerical discontinuities in the interaction region. These effects are important for predicting the ramp-wall pressure distribution, which directly contributes to the thrust-related integrated pressure quantity discussed later.

4.2 Ramp-Wall Pressure Distribution

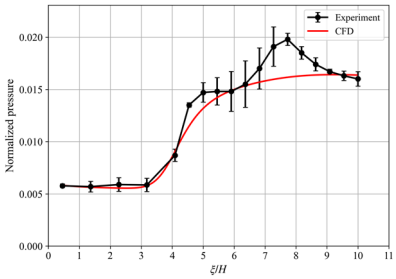
Figure 10 compares the streamwise distributions of normalized ramp-wall pressure between the experiment and the present RANS simulation. The horizontal axis is the streamwise coordinate on the test ramp, ξ, normalized by the test-nozzle exit height, H=22 mm. The vertical axis is the wall pressure, p_w, normalized by the test-nozzle total pressure, p_{0n}.

The experimental data correspond to the SAPDs (Eq. (1)) with error bars (Eq. (2)). The experimental pressure distributions show different trends depending on the expansion condition of the test-nozzle jet. Under over-expanded conditions, the normalized wall pressure first remains at a low level near the nozzle exit and then rapidly increases as the compression wave or shock wave generated from the nozzle-lip region impinges on the ramp wall. The pressure subsequently reaches a peak and gradually decreases or approaches a nearly constant level downstream. This behavior indicates that the wall pressure distribution is strongly affected by the repeated reflection of pressure waves between the ramp wall and the jet boundary. Under approximately optimum-expanded conditions, the pressure variation caused by the nozzle-lip wave system becomes weaker. The ramp-wall pressure distribution therefore exhibits a smaller streamwise variation than that observed in the strongly over-expanded cases. Under under-expanded conditions, the ramp-wall pressure gradually decreases downstream because of the expansion wave generated from the nozzle-lip region. This trend becomes more pronounced as *NPR* increases, reflecting the larger static-pressure mismatch between the test-nozzle jet and the facility-nozzle flow.

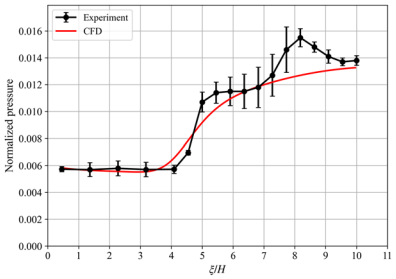
The present RANS simulation reproduces these major experimental trends over the wide *NPR* range. In particular, the calculation captures the rapid pressure rise in the over-expanded cases, the relatively weak pressure variation near the optimum-expanded condition, and the gradual pressure decrease in the under-expanded cases. These results indicate that the present simulation can predict the dominant pressure-wave structures governing the ramp-wall pressure distribution. However, some quantitative discrepancies remain. In the over-expanded cases, the computed pressure peak tends to be lower and smoother than the experimental peak. The location of the pressure rise is reasonably reproduced, but the maximum pressure level is underestimated in several cases. This discrepancy may be related to the modeling of shock-wave/boundary-layer interaction, turbulent shear-layer development, and the two-dimensional approximation used in the present computation. In the experiment, spanwise non-uniformity and side-wall effects can generate additional pressure variations that are not represented in the two-dimensional simulation. In the under-expanded cases, the overall decreasing trend of wall pressure is well reproduced by the computation. The agreement between experiment and CFD becomes better at higher *NPR*, where the wall-pressure distribution is dominated



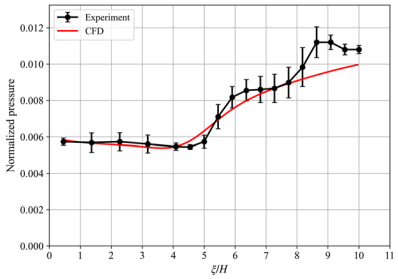
a – Cae 1, *NPR*=26.8.



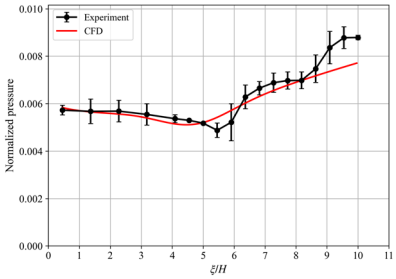
b – Cae 2, *NPR*=36.3.



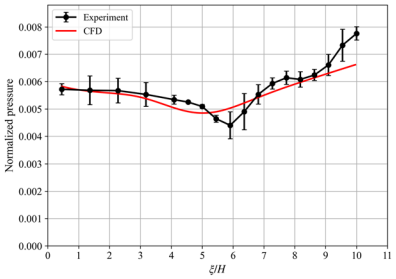
c – Cae 3, *NPR*=44.4.



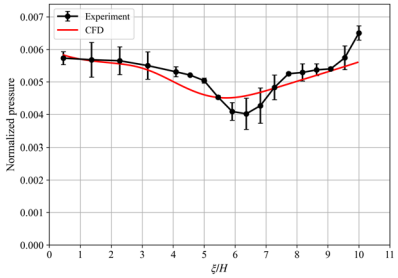
d – Cae 4, *NPR*=55.8.



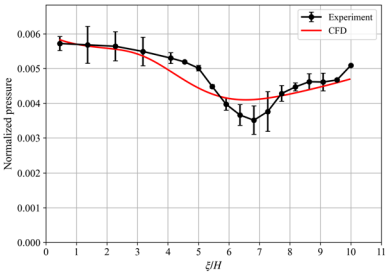
e – Cae 5, *NPR*=66.3.



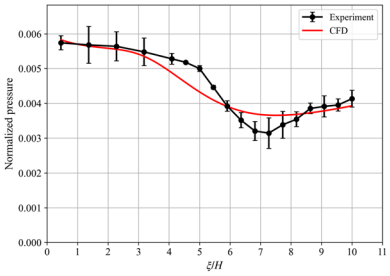
f – Cae 6, *NPR*=72.9.



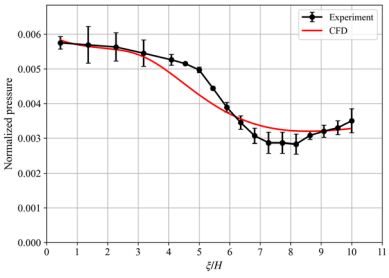
g – Cae 7, *NPR*=80.5.



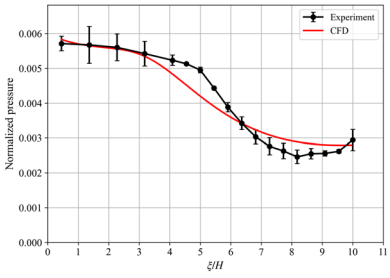
h – Cae 8, *NPR*=89.2.



i – Cae 9, *NPR*=99.1.



j – Cae 10, *NPR*=110.4.



k – Cae 11, *NPR*=122.5.

Figure 10 – Comparison of streamwise ramp-wall pressure distributions.

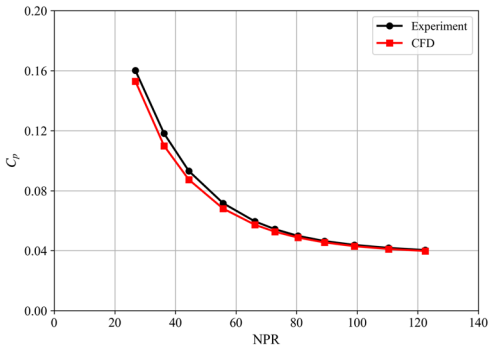


Figure 11 – Comparison of integrated pressure quantity C_p.

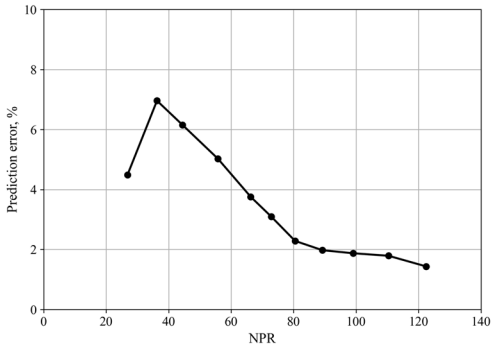


Figure 12 – Prediction error of C_p as a function of *NPR*.

by the broad expansion process rather than by a localized strong shock impingement. This suggests that the present RANS model is more reliable for predicting the integrated pressure load in under-expanded and near-optimum conditions than for resolving local pressure peaks in strongly over-expanded conditions.

4.3 Integrated Pressure Quantity Prediction

Figure 11 shows the comparison of the line-integrated pressure quantity, C_p (Eq. (3)), between the experiment and the RANS simulation as a function of *NPR*. Here, C_p is used as a thrust-related integrated quantity obtained from the streamwise ramp-wall pressure distribution. Figure 12 shows the prediction errors of C_p (Eq. (4)) under each *NPR* condition. The experimental C_p decreases monotonically with increasing *NPR*. This trend is physically reasonable because the normalized ramp-wall pressure becomes lower as the test-nozzle jet changes from over-expanded to under-expanded conditions. The present RANS simulation reproduces this monotonic decrease very well. Although the local wall-pressure peaks are not perfectly captured in some over-expanded cases, the integrated pressure quantity agrees well with the experimental data over the entire *NPR* range.

The detailed values are summarized in Table 6. The prediction error of C_p remains less than 7% for all *NPR* conditions investigated in this study. The maximum error is approximately 7.0% at *NPR*=36.3. The error decreases as *NPR* increases and becomes less than approximately 2% for NPR≥89.2. At the highest *NPR* condition, *NPR*=122.5, the prediction error is approximately 1.4%. These results indicate that the present RANS simulation provides sufficiently accurate prediction of the integrated ramp-wall pressure load for engineering-level evaluation of SEN thrust performance. The CFD result slightly underestimates C_p for all cases, which is consistent with the wall-pressure comparisons shown in Fig. 10. Nevertheless, the discrepancy is considerably smaller than that observed in the previous preliminary Euler analysis, in which the prediction error of the integrated pressure quantity was below approximately 18% [10]. The inclusion of viscous and turbulent effects in the present RANS calculation therefore improves the quantitative prediction capability.

From the viewpoint of engineering applicability, the computational cost of the present RANS approach was also evaluated. The main validation calculations were performed using the medium mesh

Table 6 – Detailed values for *Cp* derived from experiment and CFD.

Case	Expansion condition	*NPR*	$C_{p,EXP}$	$C_{p,CFD}$	*PE*, %
1	Over	26.8	0.160	0.153	4.5
2		36.3	0.118	0.110	7.0
3		44.4	0.093	0.087	6.2
4		55.8	0.072	0.068	5.0
5		66.3	0.059	0.057	3.8
6	Approximately-optimum	72.9	0.054	0.053	3.1
7		80.5	0.050	0.049	2.3
8	Under	89.2	0.046	0.045	2.0
9		99.1	0.044	0.043	1.9
10		110.4	0.042	0.041	1.8
11		122.5	0.040	0.040	1.4

selected from the mesh-sensitivity study (Table 5). The computational domain was decomposed into 11 subdomains using the scotch decomposition method, and the simulations were executed in parallel. The reported computational time corresponds to the wall-clock time obtained using 11 parallel subdomains. One calculation was completed in approximately 15 min per *NPR* condition on a laptop computer equipped with an Intel Core Ultra 7 165H CPU and 64 GB RAM, running Windows 11 with WSL2 and Ubuntu Linux. Considering that the integrated pressure quantity was predicted within an error of 7% for all *NPR* conditions, the present RANS framework provides a reasonable compromise between prediction accuracy and computational cost for preliminary SEN design applications.

4.4 Discussion on Prediction Accuracy

The present results demonstrate that the RANS simulation can reproduce both the local and integrated features of the SEN ramp-wall pressure distribution. The pressure contours indicate that the dominant pressure-wave structures generated by the interaction between the test-nozzle jet and the facility-nozzle flow are captured qualitatively. The wall-pressure comparisons further show that the calculation reproduces the characteristic *NPR* dependence of the pressure distribution. Finally, the integrated pressure quantity C_p is predicted within an error of 7% for all test cases. The remaining discrepancies can be attributed to several factors.

First, the present computation is two-dimensional, whereas the experiment inevitably includes three-dimensional effects. Although rectangular side walls were installed to suppress spanwise expansion, previous measurements showed that spanwise pressure variations still exist in this type of configuration [9]. Such three-dimensional effects can modify the local pressure-wave impingement pattern and produce pressure fluctuations that cannot be reproduced by a two-dimensional simulation.

Second, the prediction of local pressure peaks in the over-expanded cases is sensitive to the modeling of shock-wave/boundary-layer interaction, turbulent shear-layer development, and possible local flow separation. The SST k-ω model provides a robust engineering approximation for such flows, but the exact shock-induced pressure rise and the associated near-wall response may still be difficult to predict quantitatively. This is one possible reason why the computed pressure peaks are smoother and lower than those observed in the experiment. In addition, the present validation mainly focuses on the upstream ramp region before the strong influence of downstream separation becomes dominant. Therefore, the prediction of large-scale separation farther downstream is outside the main scope of the present comparison.

Third, the inlet boundary conditions were determined from the nominal wind-tunnel operating conditions and nozzle expansion assumptions. Since detailed cross-sectional measurements at the nozzle exits were not available, the actual velocity, pressure, and temperature distributions at the facility-nozzle and test-nozzle exits may differ from the prescribed inlet profiles in the computation. This uncertainty can affect the pressure-wave angle, impingement location, and wall-pressure level.

Fourth, the present computation adopted a single-gas approximation. In the experiment, the facility nozzle supplied air and the test nozzle supplied nitrogen, whereas both flows were modeled as air in the simulation because multi-species transport was not considered in the present rhoCentralFoam framework. Since the present study focuses on non-reacting aerodynamic pressure fields and normalized pressure loads, this effect is expected to be secondary compared with the uncertainties associated with boundary conditions, turbulence modeling, and three-dimensionality. Nevertheless, the gas-property difference should be regarded as one of the modeling uncertainties.

Finally, the applicability of the present cold-flow validation to actual engine conditions should be considered carefully. In an actual SEN, the flow entering the nozzle is a high-temperature combustor exhaust consisting of combustion products and possibly remaining unburned fuel. Therefore, the thermodynamic and transport properties, such as the specific heat ratio, gas constant, viscosity, and density ratio relative to the ambient flow, can differ from those in the present room-temperature non-reacting experiment. In addition, if unburned fuel remains in the exhaust, external combustion or outer burning in the nozzle plume cannot be completely excluded under certain operating conditions. Such effects may modify the jet-boundary structure, pressure-wave system, and ramp-wall pressure distribution. These high-temperature, multi-species, and reacting-flow effects are beyond the scope of the present study, which aims to validate the aerodynamic pressure prediction capability under controlled cold-flow conditions.

Overall, the present RANS simulation successfully improves the quantitative prediction of the SEN ramp-wall pressure load compared with the previous Euler-based approach. The remaining local discrepancies do not significantly degrade the prediction of the integrated pressure quantity.

Therefore, within the scope of cold-flow, non-reacting, two-dimensional aerodynamic validation, the present CFD framework is considered applicable as a practical engineering tool for preliminary estimation of SEN thrust performance over a wide *NPR* range.

5. Conclusion

In the present study, a RANS-based CFD framework was validated for predicting the thrust-related pressure load of a Scramjet External Nozzle (SEN). Wind-tunnel experimental data obtained using a Mach 3.5 test-nozzle jet and a Mach 2.0 facility-nozzle flow were used as validation data. The ramp-wall pressure distribution and its line-integrated quantity, C_p, were compared between the experiment and computation over a wide *NPR* range. The present RANS simulation qualitatively reproduced the dominant pressure-wave structures generated by the interaction between the test-nozzle jet and the facility-nozzle flow. The computed ramp-wall pressure distributions also captured the major *NPR*-dependent trends observed in the experiment, including the pressure rise in over-expanded cases and the gradual pressure decrease in under-expanded cases. The line-integrated pressure quantity, C_p, was predicted within an error of 7% for all *NPR* conditions. The maximum error was approximately 7.0% at *NPR*=36.3, and the error decreased to approximately 1.4% at *NPR*=122.5. Compared with the previous Euler-based analysis, the inclusion of viscous and turbulent effects improved the quantitative prediction accuracy of the integrated pressure load. The computational cost was also acceptable for preliminary design applications. Using the medium mesh and 11 parallel subdomains generated by the scotch decomposition method, one calculation was completed in approximately 30 min per *NPR* condition on a laptop computer. Therefore, the present RANS-based CFD framework provides a practical compromise between prediction accuracy and computational cost for engineering-level estimation of SEN thrust performance. The present study was limited to cold-flow, non-reacting, two-dimensional aerodynamic validation. Future work will extend the framework to three-dimensional high-temperature SEN flows, including multi-species gas properties and, if necessary, reacting-flow effects associated with combustor exhaust and external combustion.

6. Copyright Statement

The authors confirm that they, and/or their company or organization, hold copyright on all of the original material included in this paper. The authors also confirm that they have obtained permission, from the copyright holder of any third party material included in this paper, to publish it as part of their paper. The authors confirm that they give permission, or have obtained permission from the copyright holder of this paper, for the publication and distribution of this paper as part of the ICAS proceedings or as individual off-prints from the proceedings.

References

[1] Urzay J. Supersonic Combustion in Air-Breathing Propulsion Systems for Hypersonic Flight, *Annual Review of Fluid Mechanics*, Vol. 50, pp 593-627, 2018.

[2] Snyder C D and Pinckney S Z. A Configuration Development Strategy for the NASP, AIAA Paper 91-5044, 1991

[3] Pittman J L. A MACH 6 External Nozzle Experiment with Argon-Freon Exhaust Simulation, *SAE Trans. J. Aerosp.*, Vol. 98, No. 1, pp 1683-1691, 1989.

[4] Mitani T, Ueda S, Tani K, Sato S, Miyajima H, Matsumoto M and Yasu S. Validation studies of scramjet nozzle performance, *J. Propul. Power.*, Vol. 9, No. 5, pp 725-730, 1993.

[5] Engblom W A. Numerical Prediction of SERN Performance Using Wind Code, AIAA Paper 2003-4410, 2003.

[6] Yu Y, Xu J, Mo J and Wang M. Principal Parameters in Flow Separation Patterns of Over-Expanded Single Expansion RAMP Nozzle, *Eng. Appl. Comput. Fluid Mech.*, Vol. 8, No. 2, pp 274-288, 2014.

[7] Kunze J, Smart M K and Gollan R. A Design Method for Three-Dimensional Scramjet Nozzles with Shape Transition, *J. Propul. Power*, Vol. 38, No. 1, pp 3-17, 2022.

[8] Deng X, Tong S, Tian Y and Le J. Multi-objective optimization of scramjet nozzle under geometric constraints using a deep learning method, *Aerosp. Sci. Technol.*, Vol. 164, 110403, 2025.

[9] Isono T, Tomioka S and Sakuranaka N. An experimental investigation on effect of ambient flow on aerodynamic performances of an external nozzle, *J. Fluid Sci. Technol.*, Vol. 11, No. 1, JFST0002, 2016.

[10]Isono T. Numerical Simulation and Experimental Validation for Exhaust Flow in Scramjet External Nozzle, *Symposium on Shock Waves in Japan*, Nagoya, 1B1-1, pp 1-6, 2026 (in Japanese).

[11]Mitani T et al. SUBSCALE WIND TUNNELS AND SUPPLIMENTAL STUDIES OF SCRAMJET ENGINE TESTS, *TECHNICAL REPORT OF NATIONAL AEROSPACE LABORATORY*, TR-1458 (in Japanese).

[12]Isono T. On Effect of Cell Base Width and its Computational Modeling on Thrust Performance of a Scramjet External Nozzle, *Flow Turbulence Combust.*, Vol. 116, 32, 2026.